



1 **Impacts of Meteorological Uncertainties on the Haze Formation in Beijing-Tianjin-**
2 **Hebei (BTH) during Wintertime: A case study**

3
4 Naifang Bei¹, Jianui Wu², Tian Feng², Junji Cao², Rujin Huang², Xin Long², Li Xing², Shuyu Zhao², Xuexi Tie²,
5 and Guohui Li^{2*}

6
7 ¹School of Human Settlements and Civil Engineering, Xi'an Jiaotong University, Xi'an, Shaanxi, China

8 ²Key Lab of Aerosol Chemistry and Physics, SKLLQG, Institute of Earth Environment, Chinese Academy of
9 Sciences, Xi'an, China

10 *Correspondence to: Guohui Li (ligh@ieecas.cn)

11

12

13 **Abstract:** In the present study, a persistent heavy haze episode from 13 to 20 January 2014 in
14 Beijing-Tianjin-Hebei (BTH) is simulated using the WRF-CHEM model through ensemble
15 simulations to investigate impacts of meteorological initial uncertainties on the haze
16 formation. Model results have shown that uncertainties in meteorological initial conditions
17 substantially influence the aerosol constituent simulations at an observation site in Beijing,
18 and the ratio of the ensemble spread to ensemble mean (RESM) exceeds 50%. The ensemble
19 mean generally preforms well in reproducing the fine particles (PM_{2.5}) temporal variations
20 and spatial distributions against measurements in BTH. The initial meteorological
21 uncertainties do not alter the PM_{2.5} distribution pattern in BTH principally or dominate the
22 haze formation and development, but remarkably affect the simulated PM_{2.5} level, and the
23 RESM of PM_{2.5} concentrations can be up to 30% at the region scale. In addition, the rather
24 large RESM in PM_{2.5} simulations at the city scale also causes difficulties in implementation
25 of the control strategies. Therefore, our results suggest that the ensemble simulation is
26 imperative to avoid the impact of the initial meteorological uncertainties on the haze
27 prediction.

28

29

30

31

32



33 1 Introduction

34 Over the past three decades, rapid industrialization and urbanization have caused
35 severe air pollution in China, particularly during wintertime heavy haze with extremely high
36 levels of fine particles ($PM_{2.5}$) frequently engulfs the north of China (e.g., Chan and Yao,
37 2008; Fang et al., 2009; Zhao et al., 2013; Huang et al., 2014; Guo et al., 2014; Wu et al.,
38 2017; Li et al., 2017). Elevated atmospheric aerosols or $PM_{2.5}$ not only influence the Earth
39 climate system, but also remarkably impair visibility and potentially cause severe health
40 defects (e.g., Penner et al., 2001; Pope and Dockery, 2006; Zhang et al., 2007).

41 Meteorological condition is critical for understanding the formation, transformation,
42 diffusion, transport, and removal of the pollutants in the atmosphere. Dabberdt et al. (2004)
43 have listed the meteorological research needs for improving air quality forecasting, one of
44 which is to provide the model uncertainty information through ensemble prediction
45 capabilities and quantify uncertainties and feed-backs between meteorological and air quality
46 modeling components. Numerous studies have been performed in China to explore the role of
47 meteorological conditions in the air pollution formation (e.g., Gao et al., 2011; Zhang et al.,
48 2012; Wu et al. 2013; Wang et al. 2014; Zhang et al. 2015; Bei et al. 2016a; 2016b). Most
49 recently, Liu et al. (2017) have investigated the meteorological impacts on the $PM_{2.5}$
50 concentrations over Beijing-Tianjin-Hebei (BTH) in December 2015. Their results have
51 demonstrated that the unfavorable meteorological conditions are the main reason for
52 deterioration of the air quality in BTH, while the undertaken emission control measures have
53 only mitigated the air pollution slightly.

54 Previous studies on the air quality forecasting sensitivity to meteorological
55 uncertainties mainly include Monte Carlo simulations (e.g. Dabberdt and Miller, 2000;
56 Beekmann and Derognat, 2003) and adjoint sensitivity studies (e. g. Menut, 2003). The
57 ensemble approach has also been applied to photochemical and secondary organic aerosol



58 (SOA) simulations in various numerical models (e. g. Galmarini et al., 2004; McKeen et al.,
59 2005), photo-chemical reactions (e. g. Delle Monache and Stull, 2003), emission scenarios (e.
60 g. Delle Monache et al., 2006), physical parameterizations (e. g. Mallet and Sportisse, 2006),
61 and meteorological initial conditions (e. g. Zhang et al. 2007; Bei et al. 2012). The ensemble
62 means have generally performed better than most of individual models. Uncertainties in
63 meteorological initial conditions have been shown to substantially influence both ozone (O₃)
64 and SOA simulations, including the peak time concentrations, the horizontal distributions,
65 and the temporal variations (Zhang et al. 2007; Bei et al. 2012). Recently, Sharma et al. (2016)
66 have evaluated uncertainties in surface O₃ simulations over the South Asian region during the
67 pre-monsoon season due to different emission inventories and different chemical mechanisms.
68 They have suggested that the assessment of the tropospheric O₃ budget and its implications
69 on public health and agricultural output should be conducted prudently considering the huge
70 uncertainties caused by emission inventories and chemical mechanisms. Solazzo et al. (2017)
71 have emphasized the high interdependencies among meteorological and chemical variables
72 and the related errors, indicating that the evaluation of the air quality model performance
73 needs to be confirmed by more complementary analysis of meteorological fields and
74 chemical precursors.

75 The purpose of the present study is to explore impacts of the uncertainties in
76 meteorological initial conditions on the PM_{2.5} simulations or forecasts in BTH through
77 ensemble simulations using the WRF-CHEM model. The methodology and model are
78 presented in Section 2. The analyses, results, and discussions are included in Section 3. The
79 summary and conclusions are given in Section 4.

80

81 **2 Model and Methodology**

82 **2.1 WRF-CHEM Model**



83 A specific version of the WRF-CHEM model is used to examine impacts of the
84 uncertainties in meteorological initial conditions on the PM_{2.5} simulations or the haze
85 formation in BTH, which is developed by Li et al. (2010; 2011a, b; 2012) at the Molina
86 Center for Energy and the Environment. The model includes a new flexible gas phase
87 chemical module and the CMAQ/Models-3 aerosol module developed by US EPA
88 (Binkowski and Roselle, 2003). The inorganic aerosols are predicted using the ISORROPIA
89 Version 1.7 (Nenes et al., 1998). The SOA formation is simulated using a non-traditional
90 SOA module, including the volatility basis-set (VBS) modeling method and the SOA
91 contributions from glyoxal and methylglyoxal. Detailed description of the WRF-CHEM
92 model can be found in Li et al. (2010; 2011a, b; 2012). A persistent heavy haze pollution
93 episode from 13 to 20 January 2014 in BTH is simulated. The model simulation domain is
94 shown in Figure 1, and detailed model configurations can be found in Table 1.

95 2.2 Ensemble Initialization Method

96 The ensemble initialization method used in the present study is called “climatological
97 ensemble initialization method” in which dynamically consistent initial and boundary
98 conditions are statistically sampled from a seasonal meteorological data set (Aksoy et al.,
99 2005; Zhang et al., 2007; Bei et al. 2012). To represent the wintertime climatological
100 statistics, a data set during the period from 1 November 2013 to 28 February 2014 is
101 generated using NCEP-FNL 1°×1° reanalysis data. Thirty ensemble perturbations are
102 randomly selected from this climatological data set. Similarly, boundary conditions for each
103 ensemble member are produced from the same data set beginning at the randomly selected
104 initial time of the given member, and extended for the same length of time as the simulated
105 episode. Deviations of the initial and boundary condition data for each member from the
106 climatological mean for the entire period are then scaled down to be 20% to reduce the
107 ensemble spread to be less than typical observation error magnitudes (Nielsen-Gammon et al.,



108 2007) and added to the unperturbed initial and boundary conditions derived directly from the
109 NCEP-FNL analyses valid at 12:00 UTC on 12 January 2014, which are used for the 6-km
110 domain ensemble simulation. Figures 2a–d show the vertical distribution of the average
111 initial ensemble spread. The average spread is 0.5–3.0 m s⁻¹ for horizontal winds (U and V
112 component), 0.5–1.1 K for temperature, 0.02–0.48 hPa for pressure, and 0–0.15 g kg⁻¹ for the
113 water vapor mass mixing ratio. The initial ensemble spreads of meteorological variables are
114 generally less than their typical observation error magnitudes. It is worth noting that all the
115 ensemble simulations used the same initial and boundary conditions for chemical fields, as
116 well as the same anthropogenic emission inventory.

117 2.3 Pollutants Measurements

118 The hourly near-surface CO, SO₂, NO₂, O₃, and PM_{2.5} mass concentrations in BTH are
119 released by the China's Ministry of Environmental Protection (China MEP) and can be
120 downloaded from the website <http://www.aqistudy.cn/>. The Aerodyne High Resolution Time-
121 of-Flight Aerosol Mass Spectrometer (HR-ToF-AMS) with a novel PM_{2.5} lens is used to
122 measure the sulfate, nitrate, ammonium, and organic aerosols (OA) from 9 to 26 January
123 2014 at the Institute of Remote Sensing and Digital Earth (IRSDE), Chinese Academy of
124 Sciences (40.00°N, 116.38°E) in Beijing (Figure 1). The Positive Matrix Factorization (PMF)
125 technique is utilized to analyze the mass spectra of OA and five components are separated,
126 including hydrocarbon-like OA (HOA), cooking OA (COA), biomass burning OA (BBOA),
127 coal combustion OA (CCOA), and oxygenated OA (OOA). HOA, COA, BBOA, and CCOA
128 are interpreted as surrogates of primary OA (POA), and OOA is a surrogate of SOA. Detailed
129 information about the HR-ToF-AMS measurement can be found in Elser et al. (2016). A lidar
130 has also been deployed at IRSDE and the aerosol backscatter signal is used to retrieve the
131 planetary boundary layer (PBL) height.

132



133 3 Results and Discussions

134 3.1 Synoptic Overview

135 Figure 3 shows temporal evolutions of the observed PM_{2.5} mass concentrations
136 averaged over 13 cities (see Figure 1) in BTH during the severe haze episode from 13 to 21
137 January 2014. The observed PM_{2.5} mass concentrations are frequently more than 250 µg m⁻³
138 in the 13 cities during the episode, exceeding the standard of severe pollutions (hourly PM_{2.5}
139 mass concentration exceeding 250 µg m⁻³) according to China National Air Quality Standard
140 (Feng et al., 2016). The haze in BTH is in the stage of development from January 13 to 15,
141 with the gradual increase of the PM_{2.5} concentration. BTH is most polluted when the haze is
142 in the maturity stage on January 16, with the PM_{2.5} concentration exceeding 400 µg m⁻³ in
143 most of the cities. From January 17 to 19, the PM_{2.5} concentrations fluctuate considerably,
144 which is primarily caused by the transition between different synoptic situations. During
145 nighttime on January 19, the haze in BTH rapidly dissipates, with the PM_{2.5} concentration
146 decrease of several hundreds of µg m⁻³ in two or three hours. In addition, the diurnal cycles
147 of the observed PM_{2.5} mass concentrations are not clear, demonstrating the obvious regional
148 pollution characteristics in BTH. For the four mega-cities in BTH, The PM_{2.5} level in
149 Shijiazhuang and Baoding are much higher than Beijing and Tianjin, which is caused by the
150 massive local emissions in Shijiazhuang and Baoding.

151 NCEP-FNL reanalysis data is used in the study to examine the effect of synoptic
152 conditions on the air pollution during the haze episode in BTH. Figures s1-s3 show the
153 synoptic conditions at the surface level, 850 hPa, and 500 hPa, respectively. On January 13,
154 BTH is on the north of a high pressure at the surface level, causing the southerly wind in/on
155 the east of BTH, and sandwiched between the trough in the northeast of BTH and the high
156 pressure in the southwest of BTH at 850 hPa, inducing the westerly surface wind in the west
157 of BTH. At 500 hPa, the BTH is situated in the rear of the trough, and the westerly airflow is



158 dominant. The air pollutants in BTH are subject to be transported to the east but hindered by
159 the southerly wind, causing accumulation of air pollutants. On January 14, the high pressure
160 system begins to control BTH at the surface level and 850 hPa, and the wind is varied and
161 weak, which is favorable for the accumulation of air pollutants in BTH. On January 15, the
162 BTH is still controlled by the high pressure at the surface level and 850 hPa, and the westerly
163 wind is prevailing at the 500 hPa. The calm or weak surface wind, together with the stable
164 stratification, further facilitates accumulation of air pollutants in the BTH. On January 16, a
165 trough develops over the BTH at 850 hPa and 500 hPa, and the BTH is situated near the
166 trough line, in which the northerly and southerly wind occurs at the same time. At the surface
167 level, the northerly wind is prevailing in the north of BTH and the southerly wind is prevalent
168 in the south of BTH, leading to evacuation of air pollutants in the north of BTH and the high
169 level of air pollutants in the south of BTH. On January 17, the trough at 850 hPa commences
170 to weaken and the controlling region of the trough at 500 hPa becomes narrow. The
171 northwesterly wind is dominant over BTH, leading to divergence of the air pollutants in BTH.
172 On January 18, the BTH is located near the ridgeline at 850hPa and at the verge of the high
173 pressure at the surface level. The controlling scope of high-pressure system on the surface
174 level is wide, inducing the varied wind over the BTH and is not conducive to the evacuation
175 of air pollutants in BTH. On January 19, the prevailing southerly wind in the south of BTH
176 and the strong westerly wind in the west of BTH lead to the convergence of air pollutants at
177 the surface level. At 850 hPa and 500 hPa, BTH is situated in the southeast of the trough and
178 southwesterly wind is prevalent. On January 20, the BTH is located in the southwest of the
179 trough at 500 hPa and 850 hPa, and the strong northwesterly wind is prevailing over the BTH.
180 At the surface level, the BTH is situated between the high pressure in the west and the low
181 pressure in the east, inducing the strong northwesterly wind over BTH. The clod clean air
182 sweeps BTH and efficiently decreases the air pollutant concentrations in BTH.



183 3.2 Uncertainties in Meteorological Simulations

184 Figures 4a-d provide the temporal profiles of the ensemble simulations of the surface
185 meteorological fields and the corresponding observations at the meteorological site in Beijing
186 from 13 to 20 January 2014. The U component exhibits larger ensemble spread than the V
187 component (Figure s4), but the ensemble mean (ENSM) of the U component generally yields
188 the observed diurnal variations. The ensemble prediction of the V component fails to
189 reproduce the observed intensified southerly or northerly winds. The meteorological site is
190 located on the north of the Yanshan Mountains, substantially influenced by the mountain-
191 valley circulation (MVC). Apparently, the WRF-CHEM model lacks the ability to well
192 simulate the occurrence and development of MVC, causing the considerable biases of the
193 ensemble prediction of the V component. The ensemble prediction performs well in
194 producing the diurnal variation of the surface temperature, but the underestimation or
195 overestimation is still large when the V component prediction is biased. The relative
196 humidity (RH) shows the rather large ensemble spread (Figure s4d), and the ENSM
197 reasonably tracks the observed diurnal variation, i.e., the simulated RH is high during
198 nighttime and low in the afternoon. The RH simulation is sensitive to that of the surface
199 temperature. Generally, the overestimation of the surface temperature well corresponds to the
200 underestimation of the RH, or vice versa. The ENSM considerably overestimates the PBL
201 height during daytime on January 13 and 14, and underestimates on January 15 (Figure 4e).
202 In addition, most of the ensemble members frequently underestimate the observed PBL
203 height during nighttime, and all ensemble members fail to produce the peak PBL height on
204 January 17 and 20. The PBL height is principally determined by the vertical shear of
205 horizontal winds and the ground thermal condition. Therefore, uncertainties of wind and
206 temperature field simulations cause large biases of the PBL height simulation.

207 3.3 Uncertainties in Aerosol Species Simulations



208 Figure 5 shows the temporal profiles of the ensemble simulations of the aerosol species
209 and the observations at IRSDE in Beijing. The ENSM reasonably produces the observed
210 variations of the POA concentrations. However, all ensemble members fail to capture the
211 peaks in the morning on January 16 and in the evening on January 17, indicating that the
212 underestimation might not be caused by the meteorological uncertainties, but by the emission
213 biases. The POA in the atmosphere are contributed by multi sources, including the direct
214 emissions from vehicles, cooking, biomass and coal combustion. Diurnal variations of those
215 sources might constitute one of the major reasons for the biases of the POA simulations. The
216 ENSM generally performs reasonably well in simulating the SOA concentration against the
217 measured OOA. The ratio of the ensemble spread to the ensemble mean (RESM) for the SOA
218 prediction is large compared to that of POA (Figures s5a, b). Four SOA formation pathways
219 are included in simulations: oxidations of anthropogenic and biogenic volatile organic
220 compounds (VOCs), oxidation and partition of HOA treated as semi-volatile, and irreversible
221 uptake of glyoxal and methylglyoxal on aerosol surfaces. Therefore, uncertainties in
222 meteorological fields not only influence the transport of the SOA precursors but also the
223 SOA formation processes in the atmosphere, causing the rather large RESM of SOA
224 simulations. The ENSM generally reproduces the observed variations of sulfate, nitrate and
225 ammonium (SNA), but the RESM of SNA is also considerably large (Figures s5c-d). During
226 haze days, sulfate is primarily formed through heterogeneous reactions of SO₂ on aerosol
227 surfaces, which is highly dependent on the relative humidity (Li et al., 2017). Nitrate
228 formation is determined by the HNO₃ and N₂O₅ originated from the NO₂ oxidation, sensitive
229 to the temperature and relative humidity and also influenced by the level of sulfate in the
230 particle phase and ammonia in the atmosphere. The ammonium aerosol is formed through
231 neutralization of sulfate and nitrate aerosols by NH₃. Additionally, in the present study,
232 ISORROPIA (Version 1.7) is used to calculate the thermodynamic equilibrium between the



233 sulfate-nitrate-ammonium-water aerosols and their gas phase precursors $\text{H}_2\text{SO}_4\text{-HNO}_3\text{-NH}_3\text{-}$
234 water vapor. Therefore, uncertainties of meteorological fields propagate to the transport,
235 atmospheric oxidation, and thermal dynamic processes, which all have contributions to the
236 large RESM of the SNA simulations. Apparently, uncertainties in meteorological initial
237 conditions substantially affect the aerosol species simulations at a single observation site,
238 which is consistent with the previous studies (Bei et al., 2012).

239 3.4 Uncertainties in $\text{PM}_{2.5}$ Simulations in BTH

240 Heavy haze with high levels of $\text{PM}_{2.5}$ frequently constitutes a regional pollution event,
241 so Figure 6 shows the temporal profiles of the ensemble simulations and observations of air
242 pollutants averaged at the monitoring sites in BTH from 13 to 20 January 2014. The RESM
243 of the average air pollutants is much less than those of aerosol species at the single
244 observation site (Figure s6). For the primary air pollutants, SO_2 and CO, the ENSM generally
245 tracks reasonably the observed variations. However, sometimes all the ensemble members
246 underestimate or overestimate the observation. There are two possible reasons for the biases
247 of ensemble simulations of SO_2 and CO: uncertainties of emissions and systematic errors of
248 meteorological fields. In the evening on January 15, the ensemble prediction substantially
249 overestimates the observed SO_2 concentration, but CO overestimation is not large. In the
250 contrast, in the morning on January 16, the ensemble prediction slightly underestimates the
251 SO_2 observation but remarkably underestimates the CO concentration. Therefore, the
252 overestimation of SO_2 on January 15 and underestimation of CO on January 16 might be
253 primarily contributed by the emission uncertainties. In the morning on January 18, the
254 ensemble prediction significantly underestimates both SO_2 and CO observations, indicating
255 the plausible uncertainties caused by the systematic errors of meteorological fields.

256 The ENSM of the average surface O_3 and NO_2 over the monitoring sites in BTH is in
257 good agreement with observations. The ensemble prediction is subject to underestimate the



258 O₃ observation during nighttime, but well consistent with the NO₂ observation. Considering
259 the massive NO_x emission and the titration of NO, the nighttime O₃ concentrations are
260 generally very low, particularly during wintertime when the daytime O₃ concentrations are
261 not high. Hence, the underestimation of nighttime O₃ concentrations is perhaps caused by the
262 observation uncertainties, such as the setting of lower detection limit. In addition, the ENSM
263 does not reproduce the high O₃ level during nighttime on January 19 when the northwesterly
264 wind is intensified to evacuate the air pollutants in BTH. Rapid increase of the observed O₃
265 concentrations during nighttime shows the substantial contribution of the background O₃
266 transport. Therefore, the background O₃ uncertainties constitute the major reason for the O₃
267 underestimation on January 19.

268 The ENSM also exhibits good performance in replicating the observed PM_{2.5}
269 observation, except the underestimation on January 16 and 18. However, the RESM of the
270 PM_{2.5} simulations is larger than those of O₃, NO₂, SO₂, and CO (Figure s6). The average
271 ENSM of the PM_{2.5} concentration over the monitoring sites during the simulation period is
272 189.5 μg m⁻³, close to the observed 197.6 μg m⁻³. In addition, the ensemble member of 16
273 and 30 (EN-16 and EN-30, respectively) produces the highest and lowest PM_{2.5} level, with
274 the average PM_{2.5} concentrations of 231.5 and 167.3 μg m⁻³, respectively. The PM_{2.5} mainly
275 include the primary aerosols which are determined by direct emissions, and the secondary
276 aerosols which are determined by their precursors emissions and the homogeneous and
277 heterogeneous oxidation process in the atmosphere. Therefore, the large RESM of SOA and
278 SNA simulations enhances the ensemble spread of the PM_{2.5} simulations.

279 Figure 7 presents the spatial distributions of ENSM and observations of the daily
280 average near-surface PM_{2.5} mass concentrations during the haze episode, along with the
281 simulated wind fields. The ENSM predicted PM_{2.5} spatial patterns are generally in good
282 agreement with the observations at the ambient monitoring sites in BTH. The ENSM



283 successfully reproduces the haze development and maturity stages from January 13 to 16,
284 2014. From January 17 to 18, the northeasterly wind develops and decreases the $PM_{2.5}$ level
285 in BTH, but not strong enough to evacuate the air pollutants. The $PM_{2.5}$ pattern of ENSM is
286 well consistent with observations, but on January 18, the $PM_{2.5}$ concentrations are remarkably
287 underestimated in four cities in BTH. On January 19, the westerly wind is prevailing in BTH,
288 causing the divergence of the $PM_{2.5}$. On January 20, the intensified northwesterly wind
289 commences to empty the $PM_{2.5}$ in BTH. However, apparently, the occurrence of the
290 intensification of the northwesterly wind is early, causing considerable underestimation of the
291 $PM_{2.5}$ concentration in the ENSM.

292 The uncertainties of initial meteorological fields are generally less than observational
293 and analysis errors, but the ensemble simulations still exhibit considerable spreads. In order
294 to contrast the $PM_{2.5}$ simulations of different ensemble members, we have selected two
295 members: EN-16 and EN-30, representing the highest and lowest $PM_{2.5}$ simulations in BTH,
296 respectively. Figure 8 provides the horizontal distributions of the daily average surface $PM_{2.5}$
297 concentrations along with surface winds during the episode in EN-16 and EN-30. Similar
298 $PM_{2.5}$ distribution patterns are simulated in EN-16 and EN-30, showing that the initial
299 meteorological uncertainties do not dominate the haze formation and development principally.
300 The $PM_{2.5}$ level in EN-16 is much higher than that in EN-30 in BTH, which is mainly caused
301 by the considerable discrepancies in the surface winds between the two members. The
302 simulated southerly wind in EN-16 is generally more intense than that in EN-30, but the
303 northerly wind in EN-16 is weak compared to EN-30, which is more favorable for the air
304 pollutants accumulation in EN-16 than EN-30. On January 13 and 14, the winds in EN-30 are
305 weak or calm in BTH and the $PM_{2.5}$ is mainly attributed to the local production. However, in
306 EN-16, the prevailing south winds also deliver the air pollutants from the south areas to BTH,
307 substantially enhancing the $PM_{2.5}$ level. On January 15, although EN-16 and EN-30 both



308 produce the prevailing southerly wind in BTH, the westerly wind in EN-30 is intense
309 compared to EN-16, considerably decreasing the $PM_{2.5}$ level in EN-30. On January 16, the
310 northeasterly wind in EN-30 is intensified and evacuates the $PM_{2.5}$ in the north of BTH.
311 However, in EN-16, the simulated northeasterly wind is weak and the $PM_{2.5}$ level in the north
312 of BTH still remains high. On January 17, the simulated northerly wind in EN-16 is weak
313 compared to that in EN-30, causing higher $PM_{2.5}$ concentration in EN-16 than EN-30 in BTH.
314 On January 18, the intensified southerly wind in EN-16 considerably increases the $PM_{2.5}$
315 level in BTH compared to EN-30. On January 19, the westerly wind is prevalent in EN-30
316 and the $PM_{2.5}$ level commences to decrease, but in EN-16, the southwesterly wind still causes
317 high $PM_{2.5}$ concentrations in BTH. On January 20, the stronger northeasterly wind in EN-30
318 more efficiently evacuates the $PM_{2.5}$ than that in EN-16.

319 **3.5 Uncertainties in $PM_{2.5}$ Simulations in Mega-cities**

320 EN-16 and EN-30 both predict the haze occurrence and development in BTH during
321 the episode, although the difference of the $PM_{2.5}$ level between those two members are
322 considerable, showing that the initial meteorological uncertainties do not dominate the
323 regional haze formation. Previous studies have shown that the meteorological uncertainties
324 substantially impact the air quality simulations at the city-scale (Bei et al., 2012). Figure 10
325 presents the temporal variation of the ensemble simulations and observations averaged at four
326 mega-cities in BTH during the episode. The ENSM of the $PM_{2.5}$ concentrations in Beijing,
327 Tianjin, and Baoding is in good agreement with the observation. However, the ENSM
328 remarkably underestimates the observed $PM_{2.5}$ concentration in Shijiazhuang from January
329 16 to 19, which is hardly interpreted by the emission biases. The ENSM performs well in
330 simulating the $PM_{2.5}$ variations from January 13 to 15, and overestimates the observation on
331 January 20 in Shijiazhuang. One of the possible reasons for the underestimation in



332 Shijiazhuang is that the westerly wind is systematically overestimated from January 16 to 19
333 along the foothills of the Taihang Mountains, causing the haze plume to move eastwardly.

334 Although the ENSM produces reasonably well the $PM_{2.5}$ variations in the four mega-
335 cities against the measurement, the initial meteorological uncertainties still cause large
336 uncertainties of the $PM_{2.5}$ concentration (Figure s7). During the first three days of the episode,
337 the ENSM is well consistent with the observations in the four mega-cities, but the $PM_{2.5}$ level
338 discrepancy between the members with the highest and lowest $PM_{2.5}$ concentrations is rather
339 large, causing troubles for the implementation of the control strategies. For example, in
340 Shijiazhuang, the average $PM_{2.5}$ concentrations during the first three days in the members
341 with the highest and lowest $PM_{2.5}$ concentrations are 403.5 and $213.8 \mu\text{g m}^{-3}$, respectively,
342 and the difference is about $190 \mu\text{g m}^{-3}$. In Beijing, the average $PM_{2.5}$ concentrations in the
343 two members are 103.9 and $196.3 \mu\text{g m}^{-3}$. It is worth noting that, according to the Chinese air
344 quality standard released in 2012, the $PM_{2.5}$ concentration of $103.9 \mu\text{g m}^{-3}$ is defined as
345 “lightly polluted condition”, but $196.3 \mu\text{g m}^{-3}$ defined as “heavily polluted condition”. If the
346 heavy air pollution occurs, the control strategies will be implemented. Therefore, it is
347 necessary to use the ensemble simulation to avoid the impact of the initial meteorological
348 uncertainties on the haze prediction.

349

350 **4 Summary and Conclusions**

351 In the present study, the uncertainties in simulating haze formation due to
352 meteorological initial uncertainties are investigated using the WRF-CHEM model through
353 ensemble simulations. A persistent heavy haze episode occurred in BTH from 13 to 20 is
354 simulated. Climatological ensemble initialization approach is used to produce the initial and
355 boundary conditions for each ensemble member.



356 The ENSM of the aerosol constituents is generally in good agreement with the
357 observations at an observation site in Beijing, including the sharp buildup of the aerosol
358 constituents in the evening on January 15 and rapid falloff in the morning on January 20.
359 However, the ENSM considerably underestimates the observed secondary aerosols in the
360 evening on January 17. The ensemble spread is rather large for the aerosol constituent
361 simulations, and the RESM exceeds 50%, respectively.

362 The ENSM performs well in simulating the temporal variations of the average surface
363 CO, SO₂, NO₂, O₃ and PM_{2.5} mass concentrations over the monitoring sites in BTH, and the
364 RESM of the air pollutants is generally less than 30%. The RESM of PM_{2.5} simulations is
365 larger than the other air pollutants, which is due to the complicated composition of PM_{2.5},
366 including the contributions of primary and secondary aerosols. The initial meteorological
367 uncertainties do not principally dominate the haze formation and development, but
368 considerably alter the simulated PM_{2.5} level. The average PM_{2.5} difference during the episode
369 exceeds 60 µg m⁻³ between the two members with the highest and lowest PM_{2.5} simulations.

370 Although the initial meteorological uncertainties do not dominate the regional haze
371 formation, they still substantially influence the PM_{2.5} simulations at city-scale. The ENSM
372 reasonably well predicts the PM_{2.5} variations in the four mega-cities against the measurement,
373 including Beijing, Tianjin, Baoding and Shijiazhuang, but the RESM of the PM_{2.5} simulations
374 is rather large, causing troubles for the implementation of the control strategies. Therefore,
375 the ensemble simulation is needed to avoid the impact of the initial meteorological
376 uncertainties on the haze prediction.

377

378

379



380 *Acknowledgement:* Naifang Bei is supported by the National Natural Science Foundation of
381 China (no. 41275101 and no. 41430424) and the Fundamental Research Funds for the Central
382 Universities of China. Guohui Li is supported by “Hundred Talents Program” of the Chinese
383 Academy of Sciences and the National Natural Science Foundation of China (no.
384 41661144020).

385
386
387
388
389

390 **References**

- 391 Aksoy, A., Zhang, F., Nielsen-Gammon, J. W., and Epifanio, C. C.: Data assimilation with
392 the ensemble Kalman filter for thermally forced circulations, *J. Geophys. Res.*, 110,
393 D16105, doi:10.1029/2004JD005718, 2005.
- 394 Beekmann, M. and Derognat, C.: Monte Carlo uncertainty analysis of a regional-scale
395 chemistry model constrained by measurements from the Atmospheric Pollution Over the
396 Paris Area (ESQUIF) campaign, *J. Geophys. Res.*, 108, 8559,
397 doi:10.1029/2003JD003391, 2003.
- 398 Bei, N., Lei, W., Zavala, M., and Molina, L. T.: Ozone predictabilities due to meteorological
399 uncertainties in the Mexico City basin using ensemble forecasts, *Atmos. Chem. Phys.*, 10,
400 6295–6309, doi:10.5194/acp-10-6295-2010, 2010.
- 401 Bei, N., Li, G., and Molina, L. T.: Uncertainties in SOA simulations due to meteorological
402 uncertainties in Mexico City during MILAGRO-2006 field campaign, *Atmos. Chem.*
403 *Phys.*, 12, 11295–11308, doi:10.5194/acp-12-11295-2012, 2012.
- 404 Bei, N., Li, G., Huang, R., Cao, J., Meng, N., Feng, T., Liu, S., Zhang, T., Zhang, Q., and
405 Molina, L. T.: Typical synoptic situations and their impacts on the wintertime air
406 pollution in the Guanzhong basin, China, *Atmos. Chem. Phys.*, 16, 7373–7387, 2016a.
- 407 Bei, N., Xiao, B., Meng, N., and Feng, T.: Critical role of meteorological conditions in a
408 persistent haze episode in the Guanzhong basin, China, *Sci. Total Environ.*, 550, 273–284,
409 2016b.
- 410 Binkowski, F. S. and Roselle, S. J.: Models-3 Community Multiscale Air Quality (CMAQ)
411 model aerosol component: 1. Model description, *J. Geophys. Res.*, 108, 4183,
412 doi:10.1029/2001JD001409, 2003.
- 413 Chan, C. K., and Yao, X.: Air pollution in mega cities in China, *Atmos. Environ.*, 42, 1–42,
414 2008.
- 415 Delle Monache, L. and Stull, R.: An ensemble air quality forecast over western Europe
416 during an ozone forecast, *Atmos. Environ.*, 37, 3469–3474, 2003.
- 417 Delle Monache, L., Deng, X., Zhou, Y., and Stull, R.: Ozone ensemble forecasts: A new
418 ensemble design, *J. Geophys. Res.*, 111, D05307, doi:10.1029/2005JD006310, 2006.
- 419 Dabberdt, W. F., Carroll, M. A., Baumgardner, D., Carmichael, G., Cohen, R., Dye, T., Ellis,
420 J., Grell, G., Grimmond, S., Hanna, S., Irwin, J., Lamb, B., Madronich, S., Mcqueen, J.,
421 Meagher, J., Odman, T., Pleim, J., Schmid, H. P., and Westphal, D. L.: Meteorological
422 research needs for improved air quality forecasting: Report of the 11th Prospectus
423 Development Team of the U.S. Weather Research Program, *B. Am. Meteorol. Soc.*, 85,
424 563–586, 2004.
- 425 Dabberdt, W. F. and Miller E.: Uncertainty, ensembles and air quality dispersion modeling:
426 Applications and challenges, *Atmos. Environ.*, 34, 4667–4673, 2000.
- 427 Elser, M., Huang, R.-J., Wolf, R., Slowik, J. G., Wang, Q., Canonaco, F., Li, G., Bozzetti, C.,
428 Daellenbach, K. R., Huang, Y., Zhang, R., Li, Z., Cao, J., Baltensperger, U., El-Haddad,
429 I., and Prévôt, A. S. H.: New insights into PM_{2.5} chemical composition and sources in two
430 major cities in China during extreme haze events using aerosol mass spectrometry, *Atmos.*
431 *Chem. Phys.*, 16, 3207–3225, <https://doi.org/10.5194/acp-16-3207-2016>, 2016
- 432 Fang, M., Chan, C. K., and Yao, X. H.: Managing air quality in a rapidly developing nation:
433 China, *Atmos. Environ.*, 43, 79–86, 2009.



- 434 Feng, T., Li, G., Cao, J., Bei, N., Shen, Z., Zhou, W., Liu, S., Zhang, T., Wang, Y., Huang,
435 R.-J., Tie, X., and Molina, L. T.: Simulations of organic aerosol concentrations during
436 springtime in the Guanzhong Basin, China, *Atmos. Chem. Phys.*, 16, 10045–10061,
437 <https://doi.org/10.5194/acp-16-10045-2016>, 2016.
- 438 Galmarini, S., Bianconi, R., Klug, W., Mikkelsen, T., Addis, R., An-dronopoulos, S., Astrup,
439 P., Baklanov, A., Bartniki, J., Bartzis, J. C., Bellasio, R., Bompay, F., Buckley, R.,
440 Bouzom, M., Champion, H., D'Amours, R., Davakis, E., Eleveld, H., Geertsema, G. T.,
441 Glaab, H., Kollax, M., Ilvonen, M., Manning, A., Pechinger, U., Persson, C., Polreich, E.,
442 Potemski, S., Prodanova, M., Salt-bones, J., Slaper, H., Sofiev, M. A., Syrakov, D.,
443 Sørensen, J. H., Van der Auwera, L., Valkama, I., and Zelazny, R.: Ensemble dispersion
444 forecasting – Part I: Concept, approach and indicators, *Atmos. Environ.*, 38, 4607–4617,
445 2004.
- 446 Gao, Y., Liu, X., Zhao, C., and Zhang, M.: Emission controls versus meteorological
447 conditions in determining aerosol concentrations in Beijing during the 2008 Olympic
448 Games, *Atmos. Chem. Phys.*, 11, 12437–12451, doi:10.5194/acp-11-12437-2011, 2011.
- 449 Guenther, A., Karl, T., Harley, P., Wiedinmyer, C., Palmer, P. I., and Geron, C.: Estimates of
450 global terrestrial isoprene emissions using MEGAN (Model of Emissions of Gases and
451 Aerosols from Nature), *Atmos. Chem. Phys.*, 6, 3181–3210, doi:10.5194/acp-6-3181-
452 2006, 2006.
- 453 Guo, S., M. Hu, M. L. Zamora, J. Peng, D. Shang, J. Zheng, Z. Du, Z. Wu, M. Shao, L. Zeng,
454 M. J. Molina, and R. Zhang: Elucidating severe urban haze formation in China, *P. Natl.*
455 *Acad. Sci. USA*, 111, 17373–17378, 2014.
- 456 Hong, S.-Y., Dudhia, J., and Chen, S.-H.: A revised approach to ice microphysical processes
457 for the bulk parameterization of clouds and precipitation, *Mon. Wea. Rev.*, 132, 103–120,
458 2004.
- 459 Horowitz, L. W., Waters, S., Mauzerall, D. L., Emmons, L. K., Rasch, P. J., Tie, X.,
460 Lamarque, J.-F., Schultz, M. G., Tyndall, G. S., Orlando, J. J., and Brasseur, G. P.: A
461 global simulation of tropospheric ozone and related tracers: Description and evaluation of
462 MOZART, version 2, *J. Geophys. Res.*, 108, 4784, doi:10.1029/2002JD002853, 2003.
- 463 Huang, R. J., Zhang, Y. L., Bozzetti, C., Ho, K. F., Cao, J. J., Han, Y. M., Dällenbach, K. R.,
464 Slowik, J. G., Platt, S. M., Canonaco, F., Zotter, P., Wolf, R., Pieber, S. M., Brun, E. A.,
465 Crippa, M., Ciarelli, G., Piazzalunga, A., Schwikowski, M., Abbaszade, G., Schnelle-
466 Kreis, J., Zimmermann, R., An, Z. S., Szidat, S., Baltensperger, U., El Haddad, I., Prévôt,
467 A. S. H.: High secondary aerosol contribution to particulate pollution during haze events
468 in China, *Nature*, 514, 218–222, 2014.
- 469 Janjic, Z. I.: Nonsingular implementation of the Mellor-Yamada level 2.5 scheme in the
470 NCEP Meso Model, NCEP Office Note, 437, 61 pp., 2002.
- 471 Li, G., Lei, W., Zavala, M., Volkamer, R., Dusanter, S., Stevens, P., Molina, L.T.: Impacts of
472 HONO sources on the photochemistry in Mexico City during the MCMA-2006/MILAGO
473 Campaign, *Atmos. Chem. Phys.*, 10, 6551–6567, 2010.
- 474 Li, G., Bei, N., Tie, X., and Molina, L. T.: Aerosol effects on the photochemistry in Mexico
475 City during MCMA-2006/MILAGRO campaign, *Atmos. Chem. Phys.*, 11, 5169–5182,
476 10.5194/acp-11-5169-2011, 2011a.
- 477 Li, G., Zavala, M., Lei, W., Tsimpidi, A. P., Karydis, V. A., Pandis, S. N., Canagaratna, M.
478 R., and Molina, L. T.: Simulations of organic aerosol concentrations in Mexico City using



- 479 the WRF-CHEM model during the MCMA-2006/MILAGRO campaign, *Atmos. Chem.*
480 *Phys.*, 11, 3789–3809, 10.5194/acp-11-3789-2011, 2011b.
- 481 Li, G., Lei, W., Bei, N., and Molina, L. T.: Contribution of garbage burning to chloride and
482 $PM_{2.5}$ in Mexico City, *Atmos. Chem. Phys.*, 12, 8751–8761, 10.5194/acp-12-8751-2012,
483 2012.
- 484 Li, G., Bei, N., Cao, J., Wu, J., Long, X., Feng, T., Dai, W., Liu, S., Zhang, Q., and Tie, X.:
485 Widespread and persistent ozone pollution in eastern China during the non-winter season
486 of 2015: observations and source attributions, *Atmos. Chem. Phys.*, 17, 2759–2774,
487 doi:10.5194/acp-17-2759-2017, 2017.
- 488 Liu, T., Gong, S., He, J., Yu, et al.: Attributions of meteorological and emission factors to the
489 2015 winter severe haze pollution episodes in China's Jing-Jin-Ji area, *Atmos. Chem.*
490 *Phys.*, 17, 2971–2980, doi:10.5194/acp-17-2971-2017, 2017.
- 491 Mallet, V. and Sportisse, B.: Ensemble-based air quality forecasts: A multi-model approach
492 applied to ozone, *J. Geophys. Res.*, 111, D18302, doi:10.1029/2005JD006675, 2006.
- 493 Menut, L.: Adjoint modeling for atmospheric pollution process sensitivity at regional scale, *J.*
494 *Geophys. Res.*, 108, 8562, doi:10.1029/2002JD002549, 2003.
- 495 McKeen, S., Wilczak, J., Grell, G., Djalalova, I., Peckham, S., Hsie, E.-Y., Gong, W.,
496 Bouchet, V., Menard, S., Moffet, R., McHenry, J., McQueen, J., Tang, Y., Carmichael, G.
497 R., Pagowski, M., Chan, A., Dye, T., Frost, G., Lee, P., and Mathur, R.: Assessment of an
498 ensemble of seven realtime ozone forecasts over eastern North America during the
499 summer of 2004, *J. Geophys. Res.*, 110, D21307, doi:10.1029/2005JD005858, 2005.
- 500 Nenes, A., Pandis, S. N., and Pilinis, C.: ISORROPIA: A new thermodynamic equilibrium
501 model for multiphase multicomponent inorganic aerosols, *Aquat. Geochem.*, 4, 123–152,
502 10.1023/a:1009604003981, 1998.
- 503 Penner, J. E. et al. Aerosols, their direct and indirect effects, in: *Climate Change 2001: The*
504 *Scientific Basis, Contributions of Working Group I to the Third Assessment Report of the*
505 *Intergovernmental Panel on Climate Change*, edited by: Houghton, J. T., Ding, Y., Griggs,
506 D. J., Noguer, M., van der Linden, P. J., Dai, X., Maskell K., and Johnson, C. A.,
507 Cambridge University Press, Cambridge, UK, and New York, NY, USA, 289–348, 2001.
- 508 Pope III, C. A. and Dockery, D. W.: Health effects of fine particulate air pollution: Liens that
509 connect, *J. Air. Waste Manage.*, 56, 709–742, 2006.
- 510 Sharma, A., Ojha, N., Pozzer, A., Mar, K. A., Beig, G., Lelieveld, J., and Gunthe, S., WRF-
511 Chem simulated surface ozone over South Asia during the pre-monsoon: Effects of
512 emission inventories and chemical mechanisms, *Atmos. Chem. Phys. Discuss.*,
513 doi:10.5194/acp-2016-1083, in review, 2016.
- 514 Nielsen-Gammon, J. W., McNider, R. T., Angevine, W. M., White, A. B., and Knupp, K.:
515 Mesoscale model performance with assimilation of wind profiler data: Sensitivity to
516 assimilation parameters and network configuration. *J. Geophys. Res.*, 112, D09119,
517 doi:10.1029/2006JD007633, 2007.
- 518 Solazzo, E., Bianconi, R., Hogrefe, C., Curci, G., Tuccella, P., Alyuz, U., Balzarini, A., Baró,
519 R., Bellasio, R., Bieser, J., Brandt, J., Christensen, J. H., Colette, A., Francis, X., Fraser,
520 A., Vivanco, M. G., Jiménez-Guerrero, P., Im, U., Manders, A., Nopmongkol, U.,
521 Kitwiroon, N., Pirovano, G., Pozzoli, L., Prank, M., Sokhi, R. S., Unal, A., Yarwood, G.,
522 and Galmarini, S.: Evaluation and error apportionment of an ensemble of atmospheric



- 523 chemistry transport modeling systems: multivariable temporal and spatial breakdown,
524 Atmos. Chem. Phys., 17, 3001–3054, <https://doi.org/10.5194/acp-17-3001-2017>, 2017.
- 525 Wang, H., Xu, J., Zhang, M., Yang, Y., Shen, X., Wang, Y., Chen, D., Guo, J.: A study of the
526 meteorological causes of a prolonged and severe haze episode in January 2013 over
527 central-eastern China, Atmos. Environ., 98, 146–157, 2014.
- 528 Wu, J., Li, G., Cao, J., Bei, N., Wang, Y., Feng, T., Huang, R., Liu, S., Zhang, Q., and Tie, X.:
529 Contributions of trans-boundary transport to summertime air quality in Beijing, China,
530 Atmos. Chem. Phys., 17, 2035–2051, doi:10.5194/acp-17-2035-2017, 2017.
- 531 Wu, M., Wu, D., Fan, Q., Wang, B. M., Li, H. W., and Fan, S. J.: Observational studies of the
532 meteorological characteristics associated with poor air quality over the Pearl River Delta
533 in China, Atmos. Chem. Phys., 13, 10755–10766, doi:10.5194/acp-13-10755-2013, 2013.
- 534 Zhang, F., Bei, N., Nielsen-Gammon, J. W., Li, G., Zhang, R., Sturart, A. L., and Aksoy, A.:
535 Impacts of meteorological uncertainties on ozone pollution predictability estimated
536 through meteorological and photochemical ensemble forecasts, J. Geophys. Res., 112,
537 D04304, doi:10.1029/2006JD007429, 2007.
- 538 Zhang, J. P., Zhu, T., Zhang, Q. H., Li, C. C., Shu, H. L., Ying, Y., Dai, Z. P., Wang, X., Liu,
539 X. Y., Liang, A. M., Shen, H. X., and Yi, B. Q.: Impact of circulation patterns on
540 transport paths and air quality, Atmos. Chem. Phys., 12, 5031–5053, 2012.
- 541 Zhang, Q., Streets, D. G., Carmichael, G. R., He, K. B., Huo, H., Kannari, A., Klimont, Z.,
542 Park, I. S., Reddy, S., Fu, J. S., Chen, D., Duan, L., Lei, Y., Wang, L. T., and Yao, Z. L.:
543 Asian emissions in 2006 for the NASA INTEX-B mission, Atmos. Chem. Phys., 9, 5131–
544 5153, 2009.
- 545 Zhang, Q., Quan, J., Tie, X., Li, X., Liu, Q., Gao, Y., and Zhao, D.: Effects of meteorology
546 and secondary particle formation on visibility during heavy haze events in Beijing, China,
547 Sci. Total Environ., 502, 578–584, 2015.
- 548 Zhang, R., Li, G., Fan, J., Wu, D. L., and Molina, M. J.: Intensification of Pacific storm track
549 linked to Asian pollution, P. Natl. Acad. Sci. USA, 104, 5295–5299, 2007.
- 550 Zhao, X. J., Zhao, P. S., Xu, J., Meng, W., Pu, W. W., Dong, F., He, D., and Shi, Q. F.:
551 Analysis of a winter regional haze event and its formation mechanism in the North China
552 Plain, Atmos. Chem. Phys., 13, 5685–5696, 2013.
- 553
- 554
- 555
- 556
- 557



Figure Captions

558

559

560 Figure 1 WRF-CHEM simulation domain. The filled red (in BTH) and blue (outside of BTH)
561 circles represent centers of cities with ambient monitoring site. The size of the circle
562 denotes the number of ambient monitoring sites of cities. The filled black triangle and
563 rectangle denote the deployment location of the HR-ToF-AMS and the surface
564 meteorological site in Beijing.

565 Figure 2 Vertical distribution of the mean of initial ensemble spreads for (a) horizontal
566 winds (U and V components), (b) temperature, (c) pressure, and (d) water vapor
567 mixing ratio.

568 Figure 3 Observed hourly PM_{2.5} concentrations averaged in 13 cities of BTH during the
569 period from January 13 to 20, 2014. The blue, red, brown, and black lines represent
570 the observations in Beijing, Tianjin, Baoding, and Shijiazhuang, respectively. The
571 green lines denote the observations in other cities of BTH.

572 Figure 4 Temporal evolution of the surface (a) U component, (b) V component, (c)
573 temperature, and (d) relative humidity at the meteorological site, and (e) the PBL
574 height at IRSDE in Beijing from each ensemble member (thin green lines), the
575 ensemble mean (bold black line), and observations (black dots) from January 13 to
576 20, 2014.

577 Figure 5 Temporal evolution of the (a) POA, (b) SOA, (c) sulfate, (d) nitrate, and (e)
578 ammonium mass concentrations at IRSDE in Beijing from each ensemble member
579 (thin green lines), the ensemble mean (bold black line), and observations (black
580 dots) from January 13 to 20, 2014.

581 Figure 6 Temporal evolution of the (a) PM_{2.5}, (b) O₃, (c) NO₂, (d) SO₂, and (e) CO mass
582 concentrations averaged over monitoring sites in BTH from each ensemble
583 member (thin green lines), the ensemble mean (bold black line), and observations
584 (black dots) from January 13 to 20, 2014.

585 Figure 7 ENSM of the daily average surface PM_{2.5} concentration distributions (color
586 contour) along with the ENSM of the daily average surface winds (black arrows)
587 from January 13 to 20, 2014. The colored circles denote the PM_{2.5} measurements in
588 cities.

589 Figure 8 Same as Figure 7, but for the ensemble member of 16 with the highest simulated
590 PM_{2.5} concentration.

591 Figure 9 Same as Figure 7, but for the ensemble member of 30 with the lowest simulated
592 PM_{2.5} concentration.

593 Figure 10 Temporal evolution of the PM_{2.5} mass concentrations averaged in (a) Beijing, (b)
594 Tianjin, (c) Baoding, and (d) Shijiazhuang from each ensemble member (thin green
595 lines), the ensemble mean (bold black line), and observations (black dots) during
596 the period from January 13 to 20, 2014. The red and blue lines represent the
597 simulations in the members with highest and lowest PM_{2.5} concentrations,
598 respectively.

599

600

601



602 Table 1 WRF-CHEM model configurations

603

Regions	Beijing-Tianjin-Hebei (BTH)
Simulation period	January 13 to 21, 2014
Domain size	200 × 200
Domain center	39°N, 117°E
Horizontal resolution	6km × 6km
Vertical resolution	35 vertical levels with a stretched vertical grid with spacing ranging from 30 m near the surface, to 500 m at 2.5 km and 1 km above 14 km
Microphysics scheme	WSM 6-class graupel scheme (Hong and Lim, 2006)
Boundary layer scheme	MYJ TKE scheme (Janjić, 2002)
Surface layer scheme	MYJ surface scheme (Janjić, 2002)
Land-surface scheme	Unified Noah land-surface model (Chen and Dudhia, 2001)
Longwave radiation scheme	Goddard longwave scheme (Chou and Suarez, 2001)
Shortwave radiation scheme	Goddard shortwave scheme (Chou and Suarez, 1999)
Meteorological boundary and initial conditions	NCEP 1°×1° reanalysis data
Chemical initial and boundary conditions	MOZART 6-hour output (Horowitz et al., 2003)
Anthropogenic emission inventory	Developed by Zhang et al. (2009)
Biogenic emission inventory	MEGAN model developed by Guenther et al. (2006)

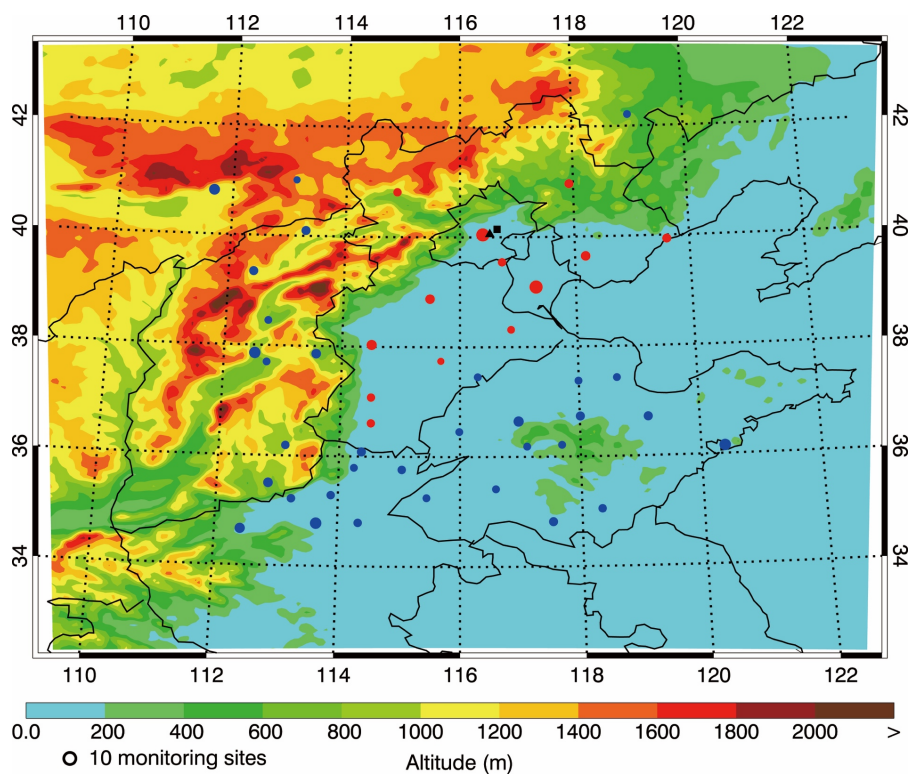
604

605

606

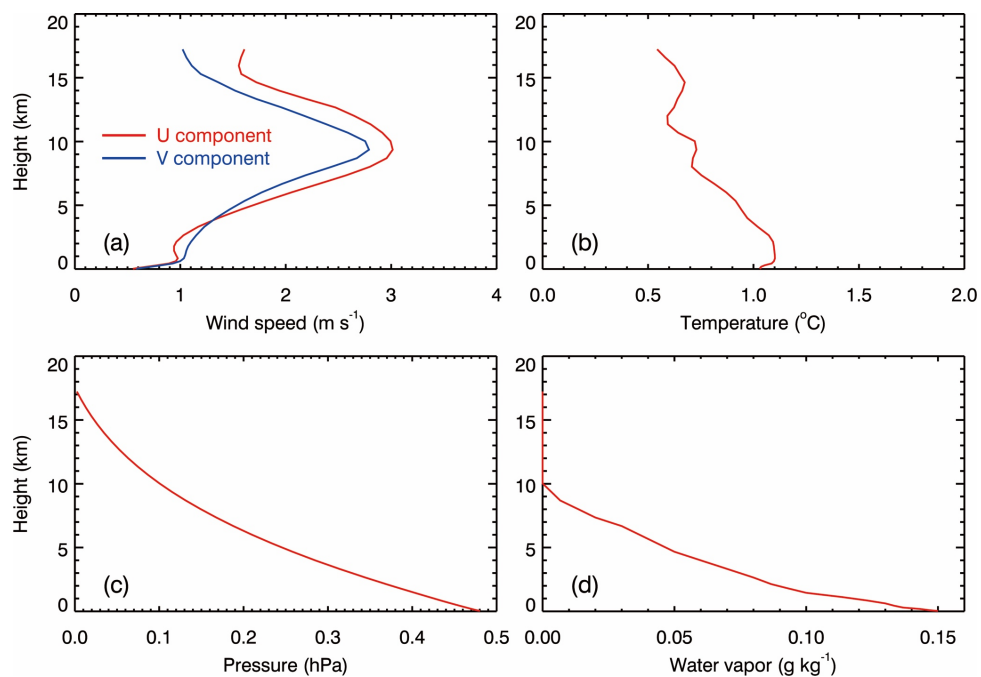
607

608



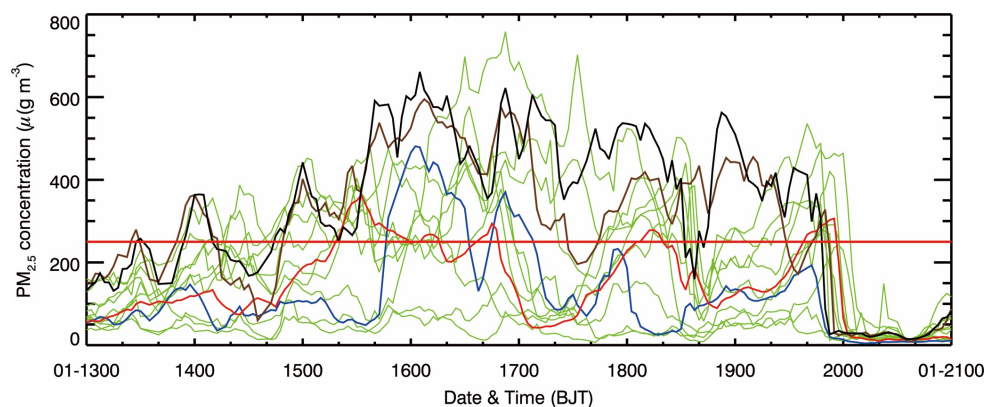
609
610
611
612
613
614
615
616
617
618
619
620

Figure 1 WRF-CHEM simulation domain. The filled red (in BTH) and blue (outside of BTH) circles represent centers of cities with ambient monitoring site. The size of the circle denotes the number of ambient monitoring sites of cities. The filled black triangle and rectangle denote the deployment location of the HR-ToF-AMS and the surface meteorological site in Beijing.



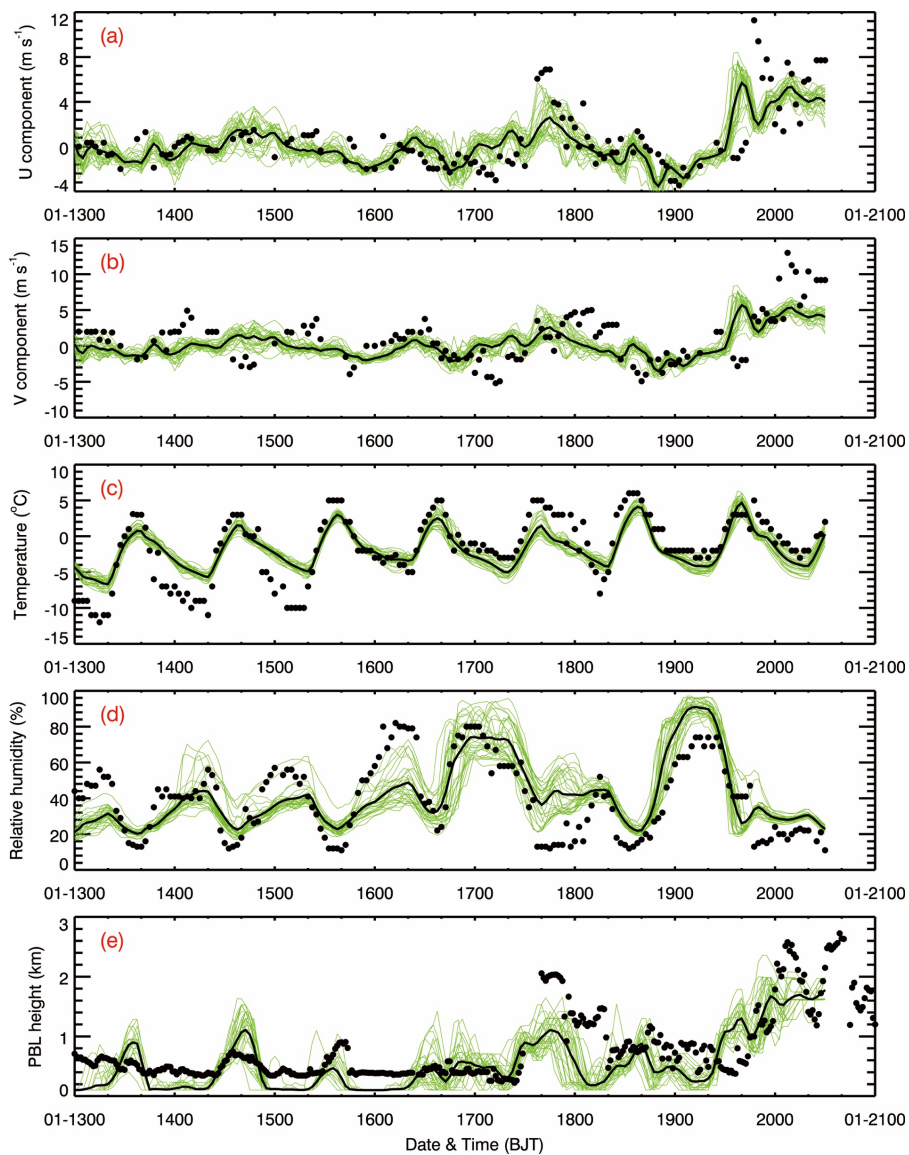
621
622
623
624
625
626
627
628
629

Figure 2 Vertical distribution of the mean of initial ensemble spreads for (a) horizontal winds (U and V components), (b) temperature, (c) pressure, and (d) water vapor mixing ratio.



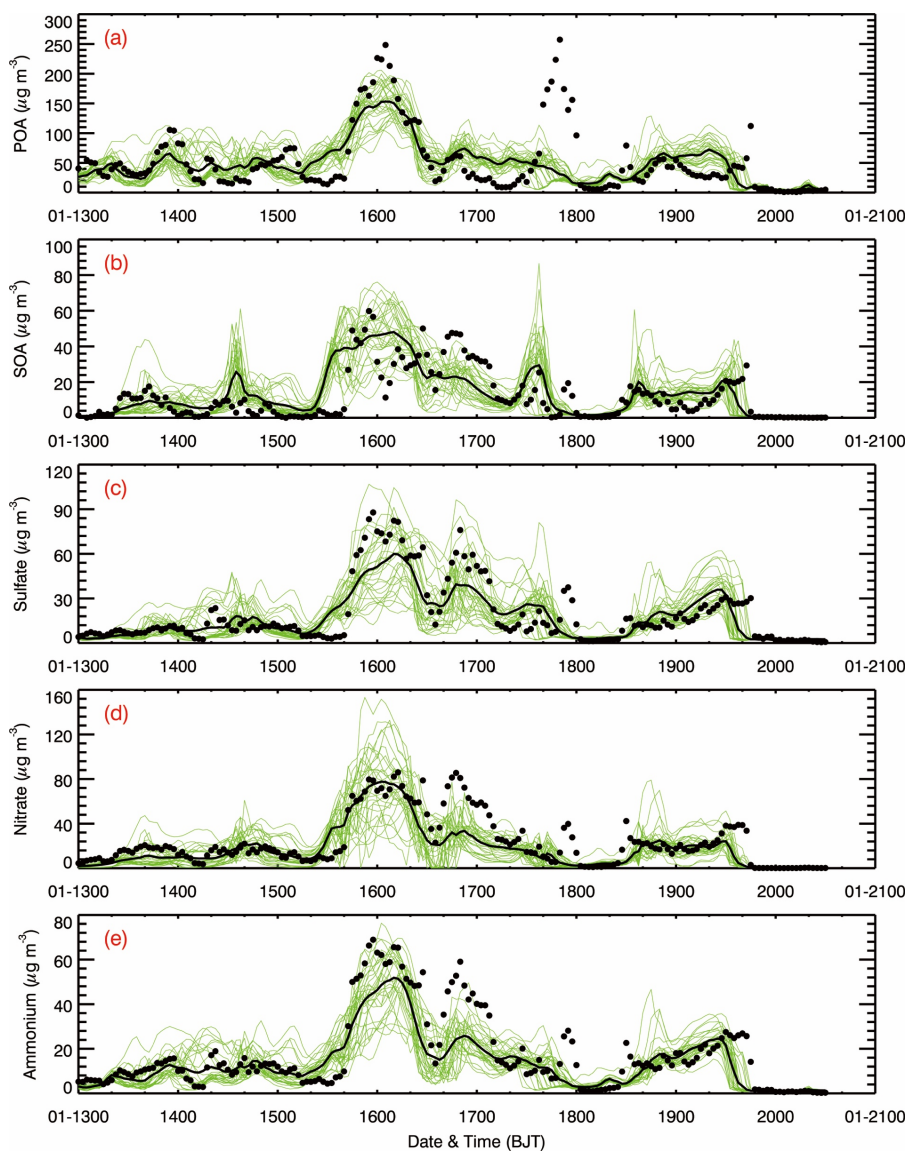
630
631
632
633
634
635
636
637
638
639
640

Figure 3 Observed hourly $PM_{2.5}$ concentrations averaged in 13 cities of BTH during the period from January 13 to 20, 2014. The blue, red, brown, and black lines represent the observations in Beijing, Tianjin, Baoding, and Shijiazhuang, respectively. The green lines denote the observations in other cities of BTH.



641
642
643
644
645
646
647
648
649
650
651

Figure 4 Temporal evolution of the surface (a) U component, (b) V component, (c) temperature, and (d) relative humidity at the meteorological site, and (e) the PBL height at IRSDE in Beijing from each ensemble member (thin green lines), the ensemble mean (bold black line), and observations (black dots) from January 13 to 20, 2014.



652

653

654 Figure 5 Temporal evolution of the (a) POA, (b) SOA, (c) sulfate, (d) nitrate, and (e)
655 ammonium mass concentrations at IRSDE in Beijing from each ensemble member (thin
656 green lines), the ensemble mean (bold black line), and observations (black dots) from January
657 13 to 20, 2014.

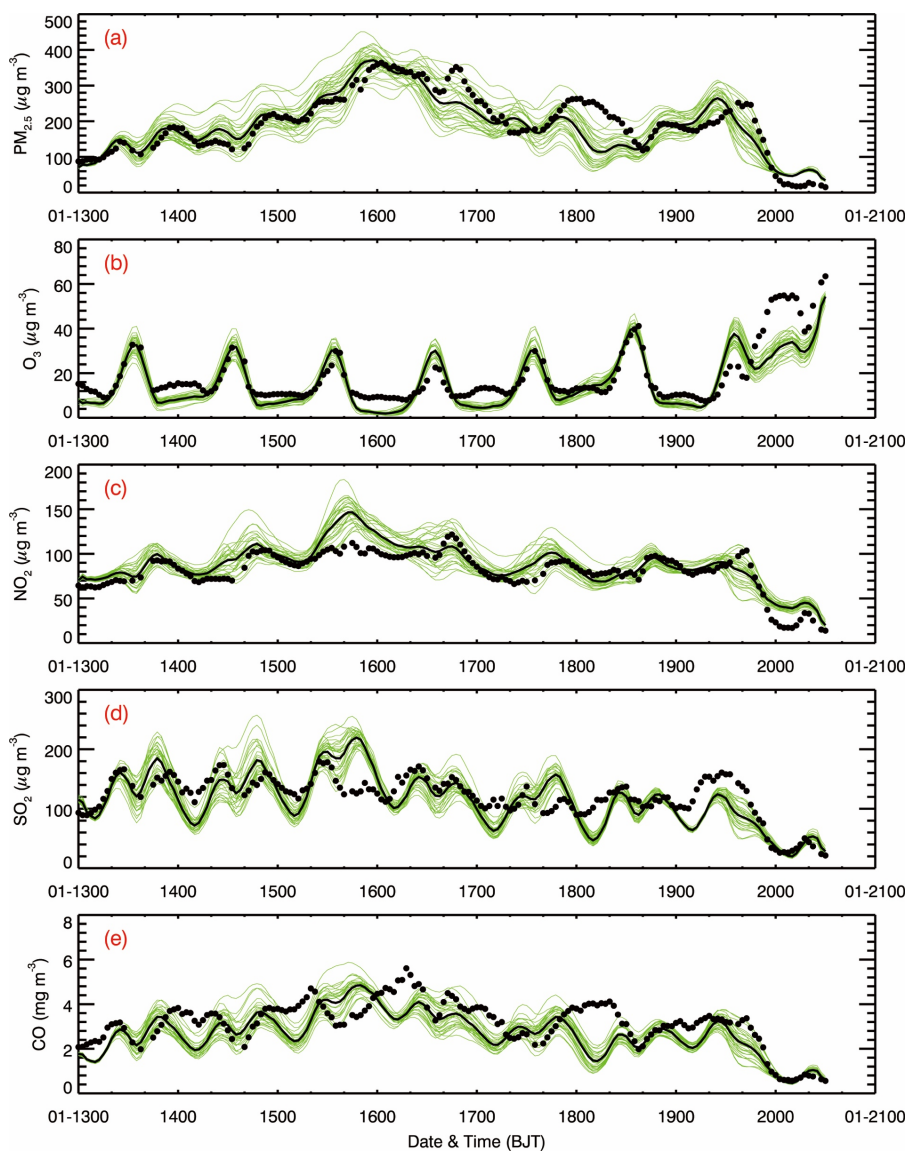
658

659

660

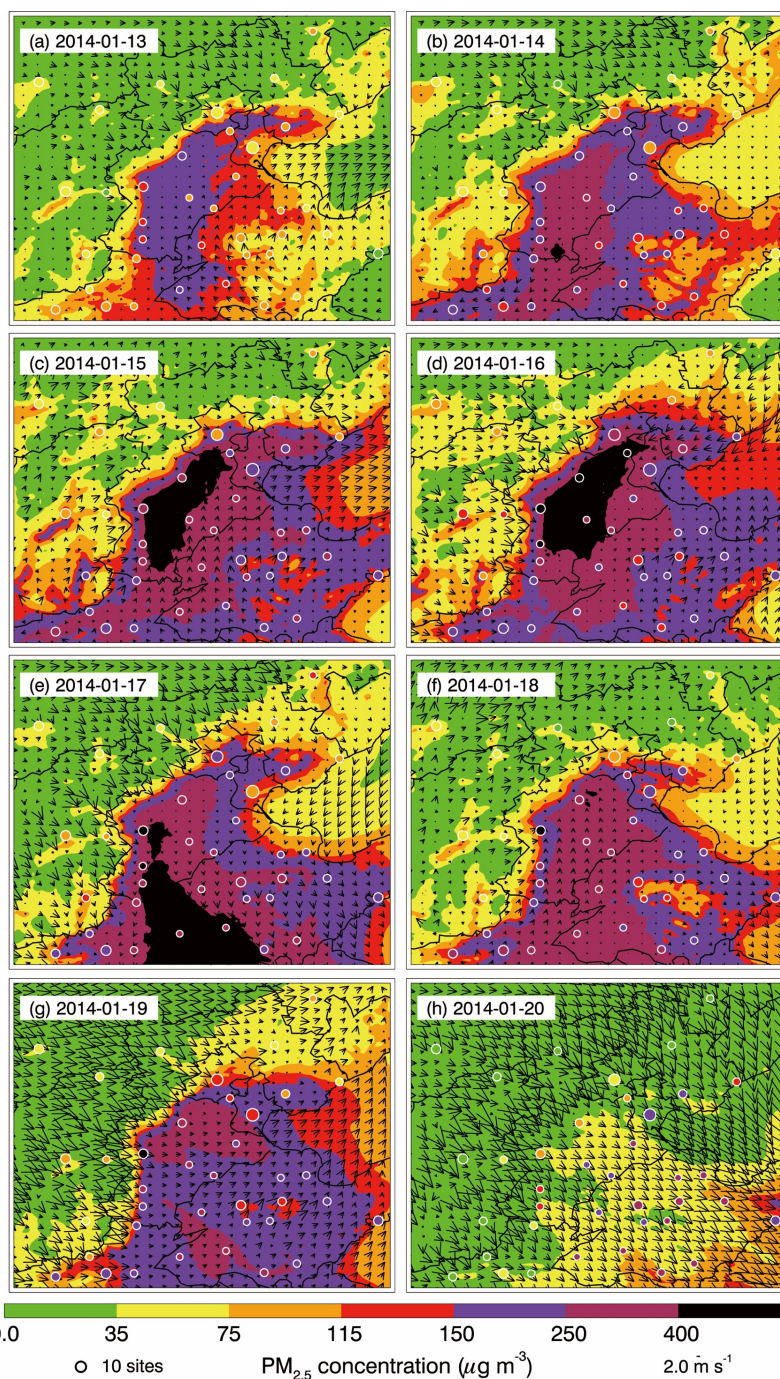
661

662

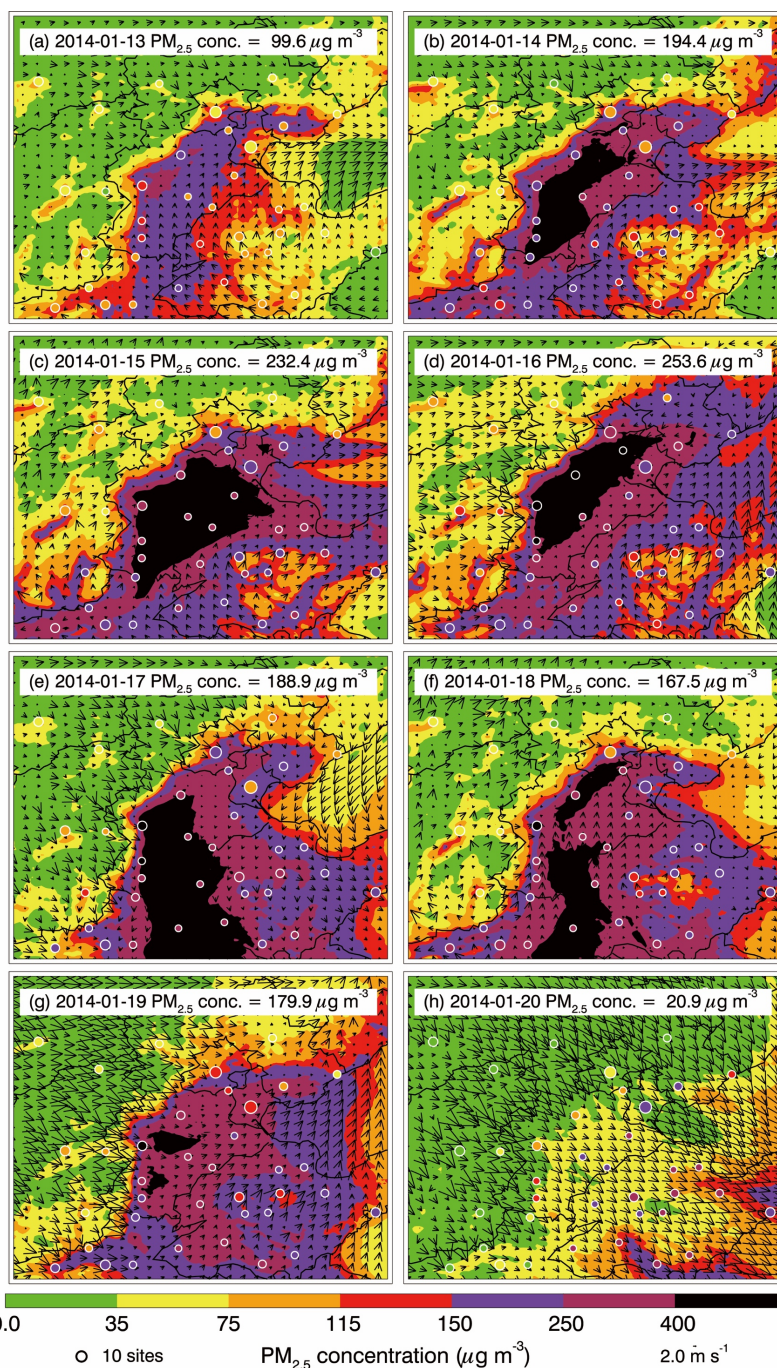


663
664
665
666
667
668
669
670
671
672
673

Figure 6 Temporal evolution of the (a) $\text{PM}_{2.5}$, (b) O_3 , (c) NO_2 , (d) SO_2 , and (e) CO mass concentrations averaged over monitoring sites in BTH from each ensemble member (thin green lines), the ensemble mean (bold black line), and observations (black dots) from January 13 to 20, 2014.



674
675 Figure 7 ENSM of the daily average surface $\text{PM}_{2.5}$ concentration distributions (colored
676 contour) along with the ENSM of the daily average surface winds (black arrows) from
677 January 13 to 20, 2014. The colored circles denote the $\text{PM}_{2.5}$ measurements in cities.
678



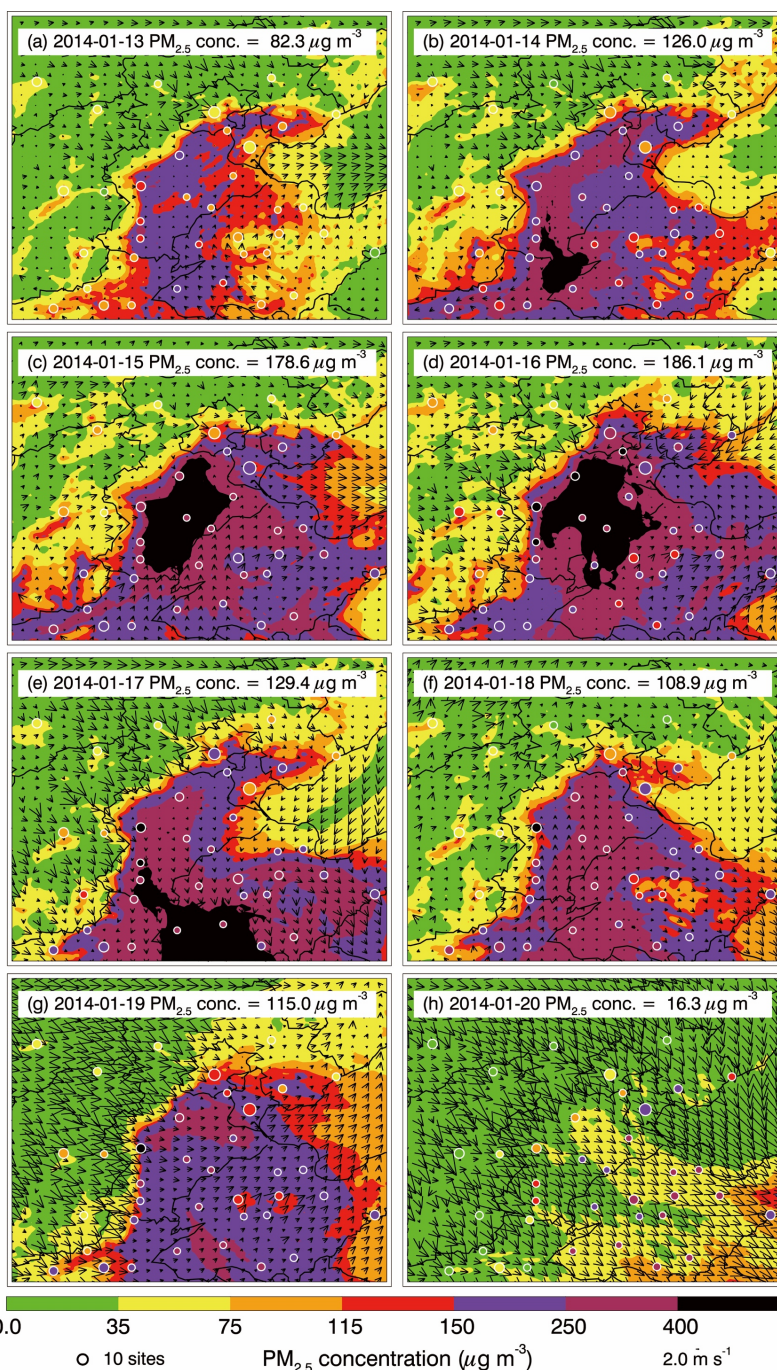
679

680 Figure 8 Same as Figure 7, but for the ensemble member of 16 with the highest simulated

681 $\text{PM}_{2.5}$ concentration.

682

683

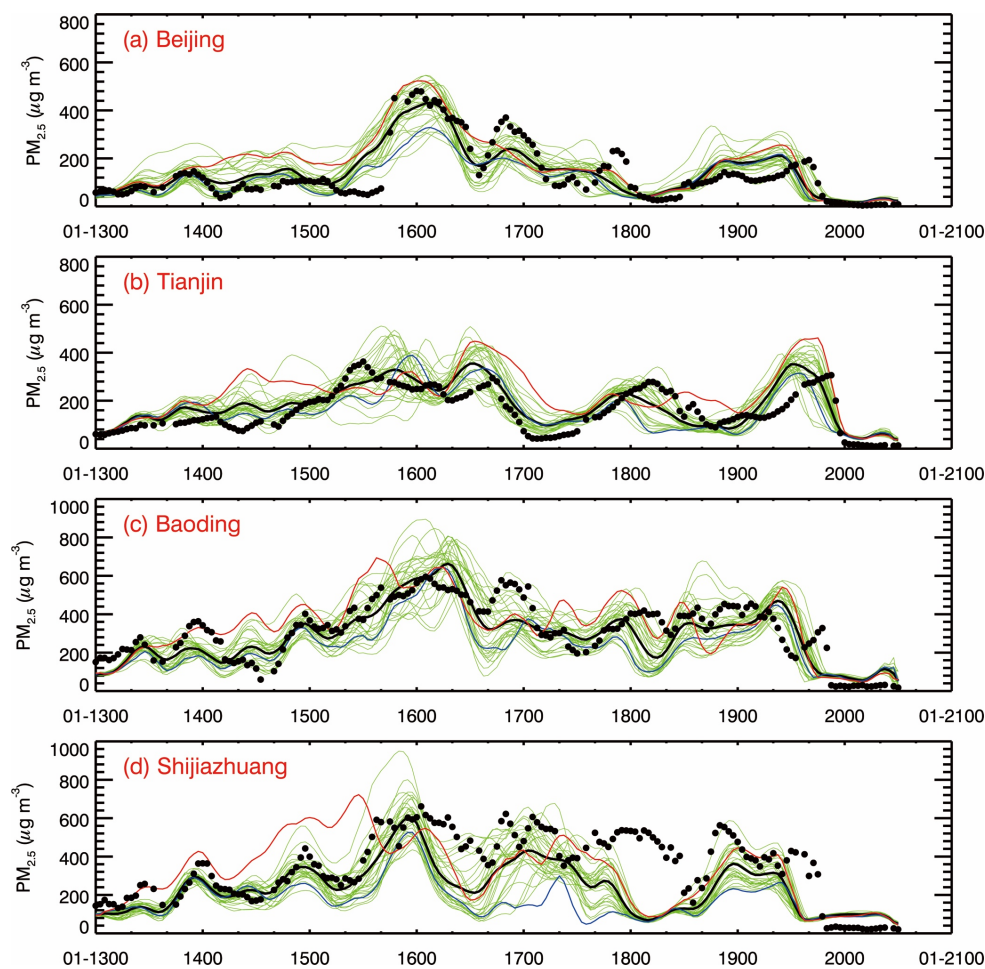


684

685 Figure 9 Same as Figure 7, but for the ensemble member of 30 with the lowest simulated
686 PM_{2.5} concentration.

687

688



689

690

691 Figure 10 Temporal evolution of the $PM_{2.5}$ mass concentrations averaged in (a) Beijing, (b)

692 Tianjin, (c) Baoding, and (d) Shijiazhuang from each ensemble member (thin green lines),

693 the ensemble mean (bold black line), and observations (black dots) during the period from

694 January 13 to 20, 2014. The red and blue lines represent the simulations in the members with

695 highest and lowest $PM_{2.5}$ concentrations, respectively.

696

697

698

699

700